A&A 553, A88 (2013)
DOI: 10.1051/0004-6361/201321289

Astronomy & Astrophysics

SABOCA 350-μm and LABOCA 870-μm dust continuum imaging of IRAS 05399-0121: mapping the dust properties of a pre- and protostellar core system⋆

O. Miettinen[1] and S. S. R. Offner[2,⋆⋆]

[1] Department of Physics, University of Helsinki, PO Box 64, 00014 Helsinki, Finland
e-mail: oskari.miettinen@helsinki.fi
[2] Department of Astronomy, Yale University, New Haven, CT 06511, USA
e-mail: stella.offner@yale.edu

Received 14 February 2013 / Accepted 25 March 2013

ABSTRACT

Context. Thermal emission from dust provides a valuable tool for determining important physical properties of the dense structures within molecular clouds.
Aims. We attempt to map the distributions of dust temperature and H_2 column density of IRAS 05399-0121/SMM 1, which is a dense double-core system in Orion B9. We also search for substructures within the cores through high-resolution submillimetre imaging.
Methods. The source was mapped with APEX/SABOCA at 350 μm. We combined these data with our previous LABOCA 870-μm data. The spatial resolution of the new SABOCA image, ~3400 AU, is about 2.6 times better than provided by LABOCA, and is therefore well-suited to our purposes. We also make use of the *Spitzer* infrared observations to characterise the star-formation activity in the source.
Results. The filamentary source remains a double-core system on the 3400 AU scale probed here, and the projected separation between IRAS 05399 and SMM 1 is 0.14 pc. The temperature map reveals warm spots towards IRAS 05399 and the southeastern tip of the source. Both IRAS 05399 and SMM 1 stand out as peaks in the column density map. A simple analysis suggests that the density profile has the form $\sim r^{-(2.3^{+2.2}_{-0.9})}$, as determined at the position of SMM 1. The broadband spectral energy distribution of IRAS 05399 suggests that it is near the Stage 0/I borderline. A visual inspection of the *Spitzer*/IRAC images provides hints of a quadrupolar-like jet morphology around IRAS 05399, supporting the possibility that it is a binary system.
Conclusions. The source splitting into two subcores along the long axis can be explained by cylindrical Jeans-type fragmentation, but the steepness of the density profile is shallower than what is expected for an isothermal cylinder. The difference between the evolutionary stages of IRAS 05399 (protostellar) and SMM 1 (starless) suggests that the former has experienced a phase of rapid mass accretion, supported by the very long outflow it drives. The protostellar jet from IRAS 05399 might have influenced the nearby core SMM 1. In particular, the temperature map features are likely to be imprints of protostellar or shock heating, while external heating could be provided by the nearby high-mass star-forming region NGC 2024.

Key words. stars: formation – stars: protostars – ISM: individual objects: IRAS 05399-0121 – submillimeter: ISM

1. Introduction

Understanding of Galactic star formation is ultimately linked to the understanding of the physical properties of dense cores in molecular clouds, because they appear to be the direct progenitors of new stars. It is well established that the formation process of low-mass (~0.1−2 $M_\odot$) solar-type stars start in gravitationally bound starless cores or so-called prestellar cores (Ward-Thompson et al. 1994). Because these sources represent the physical conditions of dense gas and dust best before the influence of star formation, they are especially useful targets for studies of the initial stages of the star-formation process. At some point, a prestellar core collapses due to its self-gravity, and, after a short (~10^2−10^3 yr) transitional first-hydrostatic core stage (Larson 1969; Masunaga et al. 1998; Bate 2011), a central protostar forms in its centre (the so-called second hydrostatic core; e.g., Masunaga & Inutsuka 2000). The emission of these young accreting sources is heavily reprocessed by the dense embedding gas and dust, and consequently they appear as cold, sub-mm sources also known as Class 0 objects (André et al. 1993, 2000).

Based on statistical estimates, the lifetime of the Class 0 stage is ~1×10^5 yr (Evans et al. 2009; Enoch et al. 2009). However, the accretion rate and duration can be highly dependent on the initial and/or environmental conditions (e.g., Vorobyov 2010; Offner et al. 2012b). Over time, the protostellar envelope dissipates through mass accretion onto the forming star and ejection of circumstellar material through outflows (e.g., Arce & Sargent 2006). The source emission shifts to shorter wavelengths, peaking in the infrared, and the object becomes a Class I source. The transition from Class 0 to Class I is thought to occur when the envelope mass is approximately equal to the mass of the central protostar. However, protostellar masses cannot be directly measured, and in practice source classification

⋆ This publication is based on data acquired with the Atacama Pathfinder EXperiment (APEX) under programmes 079.F-9313(A) and 090.F-9307(A). APEX is a collaboration between the Max-Planck-Institut für Radioastronomie, the European Southern Observatory, and the Onsala Space Observatory.
⋆⋆ Hubble Postdoctoral Fellow.

is very sensitive to the inclination of the protostellar disk and outflow (e.g., Whitney et al. 2003; Robitaille et al. 2007; Offner et al. 2012b). After the envelope is dispersed, further accretion is minimal, the source is optically revealed, and it enters the pre-main sequence (e.g., Wuchterl & Tscharnuter 2003).

The target source of the present study is a dense core system in the Orion B9 star-forming region that consists of a candidate prestellar core and a Class 0/I protostar, namely the Infrared Astronomical Satellite (IRAS; Neugebauer et al. 1984) source 05399-0121 (hereafter, I05399). This source has been the target of several previous studies, and what follows is an overview of these studies in chronological order.

Wouterloot & Walmsley (1986) searched for 22-GHz H_2O maser emission from I05399 but it was not detected. The source was also included in the NH_3 survey by Wouterloot et al. (1988), where the (1, 1) line was detected at 9.25 km s^{-1} but only an upper limit to the gas kinetic temperature of $T_{\rm kin} < 11.1$ K could be derived. The same authors later included I05399 as part of their ^{12}CO/^{13}CO survey of selected IRAS sources (Wouterloot et al. 1989). As can be seen in their Fig. 1, the ^{12}CO(1−0) line shows a blue asymmetric profile with the blue peak being 4 K stronger than the red peak. Moreover, the ^{13}CO(1−0) line peaks near the central dip of the double-peaked ^{12}CO line. This could be the signature of the infalling gas motions (e.g., Zhou 1992; Myers et al. 1996). However, it is also possible that there are just distinct velocity components along the line of sight; for example, there is additional CO isotopologue emission at ∼2.5−3 km s^{-1} (Wouterloot et al. 1989; their Fig. 1). In addition, the ^{12}CO line detected by these authors shows non-Gaussian, high-velocity wing emission of low intensity indicative of outflowing gas.

Lada et al. (1991) performed a CS(2−1) survey of the Orion B molecular cloud. The CS clump they found to be associated with I05399 (No. 30) is commonly called LBS 30 according to authors' last names. Within the 5σ emission level, the effective radius and mass of LBS 30 were determined to be 0.21 pc and 85.6 $M_\odot$ (they adopted a distance of 400 pc[1]). Further NH_3 studies of I05399 were performed by Harju et al. (1991, 1993). The NH_3(1, 1) map from Harju et al. (1993; their Appendix) shows an elongated structure where an additional ammonia condensation can be seen southeast of I05399. The average linewidth and $T_{\rm kin}$ they derived for the mapped source are 0.6 ± 0.2 km s^{-1} and 13.8 ± 3.6 K, respectively, and the mass, as estimated from NH_3, is 14 $M_\odot$ (they adopted a distance of 500 pc). Caselli & Myers (1995) mapped the Orion B9 region in the $J = 1-0$ line of ^{13}CO and C^{18}O, and I05399 was found to lie within the C^{18}O clump in the centre of the map (their Fig. 4). I05399 was also included in the large 22-GHz H_2O maser survey by Codella et al. (2002) but, similarly to Wouterloot & Walmsley (1986), no emission was detected. To our knowledge, the first millimetre dust continuum emission map of LBS 30 was made by Launhardt et al. (1996). They used both the SEST 15-m and IRAM 30-m telescopes to image the 1.3-mm dust emission of LBS 30, and found a dust core associated with I05399 and a subcore southeast of it, resembling the morphology seen in the NH_3 map by Harju et al. (1993). Assuming a distance of 400 pc and dust temperature of $T_{\rm dust} = 30$ K, Launhardt et al. (1996) estimated the total mass of the source to be 3.7 $M_\odot$. LBS 30 was included in the multitransition CS study of Lada et al. (1997). Their large velocity gradient modelling of the lines yielded a density of 2×10^5 cm^{-3} within the region where CS(5−4) line was detected, i.e., within the effective radius 0.03 pc at $d = 400$ pc. Bergin et al. (1999) mapped the source in the $J = 1-0$ line of the molecular ions N_2H^+, $H^{13}CO^+$, and DCO^+, and also in C^{18}O(1−0) and CS(2−1) (see their Fig. 1). Interestingly, the line emission of all the species peaks towards the southeastern core, rather than towards I05399. Particularly their N_2H^+ map appears very similar to that of NH_3 (Harju et al. 1993), which might not be surprising given that both species are excellent tracers of the dense interstellar gas (e.g., Bergin & Langer 1997). By utilising the molecular ion data, Bergin et al. (1999) constrained the fractional ionisation in I05399 to lie in the range $9.3 \times 10^{-8} < x(\mathrm{e}) < 1.8 \times 10^{-7}$, with the best-fit value being $\sim 1.3 \times 10^{-7}$. I05399 also appeared in the C^{18}O/$H^{13}CO^+$ survey of Aoyama et al. (2001). They designated the source as the $H^{13}CO^+$ clump No. 7, and derived the effective clump radius and mass of 0.23 pc and 18 $M_\odot$ (assuming $d = 400$ pc).

One of the most intriguing features of I05399 is the highly collimated HH 92 jet emanating from it, and the associated parsec-scale bipolar outflow discovered by Bally et al. (2002). This giant outflow, consisting of the Herbig-Haro objects HH 90, 91, 92, 93, 597, and 598, has a projected length of about 34′ (4.1 pc at 415 pc). The HH 92 jet was found to exhibit small-scale wiggles, and HH 598 at the northwestern end of the outflow was found to deviate from the current orientation of the HH 92 jet by 3° in projection. One explanation for the observed features is that I05399 is composed of a binary protostar whose orbital period modulates the outflow's mass-loss rate and velocity. Connelley et al. (2007) observed 2-μm emission features extending 1′ to the northwest of I05399. These are likely to be the result of shocked H_2 emission from the HH 92 jet. I05399 was included in the 22-GHz H_2O maser survey of IRAS sources by Sunada et al. (2007) but, similarly to the above mentioned studies, no maser emission was detected. This is consistent with the fact that among low-mass young stellar objects (YSOs), 22-GHz H_2O masers, which are collisionally pumped in shocked gas, are found to be associated with predominantly Class 0 protostars and in excited shocks of protostellar jets in the close vicinity of the central star (e.g., Furuya 2003). I05399 may have already passed through the H_2O maser phase, but also viewing geometry and variability could play a role.

I05399 was designated as the source J054227.9-012003 in the SCUBA Legacy Catalogues by Di Francesco et al. (2008). The 450- and 850-μm flux densities they reported are 26.06 and 3.62 Jy, respectively. Ikeda et al. (2009) performed an $H^{13}CO^+$(1−0) survey of dense cores in Orion B, and their core No. 56 is associated with I05399. The radius and mass they derived for this $H^{13}CO^+$ core are 52.″6 (0.12 pc) and 6.8 $M_\odot$ (at $d = 470$ pc as they assumed). The virial mass they derived, 5.8 $M_\odot$, suggests that the $H^{13}CO^+$ core is near virial equilibrium. More recently, Miettinen et al. (2009); hereafter, Paper I) mapped the whole Orion B9 region in the 870-μm dust continuum emission with the Large APEX BOlometer CAmera (LABOCA) bolometer on APEX. With the peak intensity of 0.81 Jy beam^{-1}, I05399 was found to be the second strongest 870-μm source in the region. Similarly to earlier studies, a dense starless core southeast of I05399 was detected. We suggested that it is a prestellar core and called it SMM 1. We also constructed the spectral energy distribution (SED) of I05399 by combining data from IRAS, *Spitzer* (24 and 70 μm), and LABOCA. The dust temperature and mass of the cold envelope,

[1] In the present paper, we adopt a distance of 450 pc to the Orion giant molecular cloud (Genzel & Stutzki 1989). The actual distance may be somewhat smaller as, for example, Menten et al. (2007) determined a trigonometric parallax distance of 414 ± 7 pc to the Orion Nebula. In this introduction section, however, we quote the distance values (and distance-dependent physical properties) used by different authors.

and the bolometric luminosity were found to be 18.5 ± 0.1 K, 2.8 ± 0.3 $M_\odot$, and 21 ± 1.2 $L_\odot$, respectively (d = 450 pc). Based on its SED properties, we suggested that I05399 is in a transition phase from Class 0 to I, whereas it was previously classified as a Class I object (e.g., Bally et al. 2002 and references therein). Miettinen et al. (2010; hereafter, Paper II) performed follow-up NH_3 observations of the Orion B9 cores. The gas kinetic temperature and one-dimensional non-thermal velocity dispersion towards I05399 and SMM 1 were derived to be 13.5±1.6 and 11.9±0.9 K, and 0.24 and 0.27 km s^{-1}, respectively. The latter values are transonic, i.e., $\sigma_{\rm NT} \sim c_{\rm s}$, where $c_{\rm s}$ is the isothermal sound speed. We note that the spatial resolution of our NH_3 observations, 40″ or 0.09 pc at 450 pc, corresponds to the typical size of dense cores and the sonic scale length of the interstellar medium, $\lambda_{\rm s} \sim 0.1$ pc, where turbulence transitions from supersonic to subsonic (Vázquez-Semadeni et al. 2003). Therefore, at the sonic scale we expect $\sigma_{\rm NT} \simeq c_{\rm s}$.

Employing the new temperature values with the assumption that $T_{\rm kin} = T_{\rm dust}$, the masses of I05399 and SMM 1 were estimated to be 6.1 ± 1.4 and 8.4 ± 1.5 $M_\odot$. The virial-parameter analysis of SMM 1 suggested that it is gravitationally bound, supporting our earlier speculation that it is in the prestellar phase of evolution. Miettinen (2012; hereafter, Paper III) presented further molecular-line observations towards I05399 and SMM 1. The CO depletion factors towards these sources were estimated to be 3.2 ± 0.7 and 1.9 ± 0.3, respectively. Despite the fact that no evidence of a significant CO depletion in SMM 1 was found, we derived a very high level of N_2D^+/N_2H^+ deuteration, namely 0.992 ± 0.267. On the other hand, towards I05399, the DCO^+/HCO^+ and N_2D^+/N_2H^+ column density ratios were found to be 0.020 ± 0.004 and 0.207 ± 0.046. A lower limit to the fractional ionisation of x(e) > 1.5×10^{-8} was derived in I05399, which is over six times lower than the corresponding value determined by Bergin et al. (1999). The cosmic-ray ionisation rate of H_2 was estimated to be $\zeta_{\rm H_2} \sim 2.6 \times 10^{-17}$ s^{-1}, which is within a factor of two of the standard value 1.3×10^{-17} s^{-1} (e.g., Caselli et al. 1998). We also detected D_2CO emission from both I05399 and SMM 1. We note that D_2CO, a molecule expected to form on the surface of dust grains, was also detected in starless/prestellar cores by Bacmann et al. (2003) and Bergman et al. (2011). Its presence in the gas phase requires an efficient desorption mechanism, which in starless cores could be due to cosmic-ray bombardment and/or the release of the formation energy of the newly formed species (see Paper III and references therein). However, in SMM 1 the gas-phase D_2CO could originate in shocks driven by the HH 92 jet from I05399. This conforms to the low CO depletion factor derived towards SMM 1. Overall, the results of Paper III suggest very peculiar chemical properties in the I05399/SMM 1-system.

Recent *Herschel* data show that I05399/SMM 1 is embedded in a northeast-southwest oriented filamentary structure (see Miettinen 2012; Fig. 9 therein). Miettinen (2012) found that there is a sharp velocity gradient in the region (across the short axis of the parent filament), and speculated that it might represent a shock front resulting from the feedback from the nearby expanding H II region NGC 2024. As for the other members of Orion B9, the formation of the I05399/SMM 1-system might have been triggered by this feedback. Finally, we note that I05399 is the source No. 3133 in the *Spitzer* YSO survey of Orion molecular clouds (Megeath et al. 2012), and No. 310 in the *Herschel* spectroscopic survey of protostars in Orion (Manoj et al. 2013). Manoj et al. (2013) observed far-infrared CO lines, and suggested that the emission originates in low-density gas ($n(H_2) = 6.3^{+9.5}_{-6.2} \times 10^3$ cm^{-3}) heated by outflow shocks ($T = 3\,548^{+918}_{-729}$ K) near the protostar (at radii ≳ several 100−1000 AU).

To broaden our view of the I05399/SMM 1-system and its physical properties, we mapped it in the 350-μm dust continuum emission with the Submillimetre APEX Bolometer Camera (SABOCA) on APEX. This allowed us to improve the angular resolution by a factor of about 2.6 compared to our previous LABOCA map of the source. In this paper, we discuss the results of our new high-resolution 350-μm data, and use it in conjuction with the LABOCA 870-μm data. The observations, data, and data reduction are described in Sect. 2. We present the observational results in Sect. 3, whereas analysis and its results are presented in Sect. 4. We discuss the results in Sect. 5 and in Sect. 6, we summarise the paper and draw our main conclusions.

2. Observations and data reduction

2.1. SABOCA 350-μm imaging

A field of 7.′0 × 6.′1 (0.012 deg^2), centred between I05399 and SMM 1 on the coordinates $\alpha_{2000.0} = 05^{\rm h}42^{\rm m}29\overset{\rm s}{.}6$, $\delta_{2000.0} = -01°20'19\overset{''}{.}2$, was mapped with SABOCA (Siringo et al. 2010) on the APEX 12-m telescope (Güsten et al. 2006) at Llano de Chajnantor in the Atacama desert of the Chilean Andes. This site provides very good weather conditions for submm astronomy (e.g., Tremblin et al. 2012). SABOCA is a 37-channel on-sky TES (transition edge sensor) bolometer array operating at 350 μm, with a nominal resolution of 7.″7 (HPBW). The effective field of view of the array is 1.′5. The SABOCA passband has an equivalent width of about 120 GHz centred on an effective frequency of 852 GHz. The observations were carried out on 22 and 23 August 2012. The atmospheric attenuation at 350 μm was monitored using the sky-dip method, and the zenith opacity was found to be in the range $\tau_{\rm z}^{350\,\mu{\rm m}} = 0.84-1.17$. The amount of precipitable water vapour (PWV) was ∼0.3−0.5 mm. The telescope focus and pointing were optimised and checked at regular intervals on the planets Mars and Uranus, the red supergiant VY Canis Majoris (VY CMa), FU Orionis star V883 Ori, infrared cluster NGC 2071 IR, and the massive YSO/H_2O maser source G305.80-0.24 (B13134). The absolute calibration uncertainty for SABOCA is ∼30%. Mapping was performed using a "fast-scanning" method without chopping the secondary mirror (Reichertz et al. 2001). The mosaic was constructed by combining 30 individual fast-scanning (∼1.′2−1.′5 s^{-1}) maps. The total on-source integration time was 4.2 h (during the UTC time ranges 08:42–14:02 and 15:26–16:39).

Data reduction was done with the pipeline iterations of the Comprehensive Reduction Utility for SHARC-2 (CRUSH-2, version 2.12-2) software package[2] (Kovács 2008). During the reduction process, smoothing with a Gaussian kernel of the size 1.″41 was applied. The instrument beam FWHM used in CRUSH-2 is 7.″5, so the angular resolution of the final image is 7.″63 (0.017 pc or 3 433.5 AU at 450 pc). The gridding was performed with a cell size of 1.″5. The resulting 1σ rms noise level in the final map is ∼80 mJy beam^{-1}.

2.2. LABOCA 870-μm data

Our LABOCA (Siringo et al. 2009) 870-μm observations were already published in Paper I. The data was originally reduced using the BOlometer array data Analysis software (BoA; Schuller 2012). However, to eliminate the effect of

[2] http://www.submm.caltech.edu/~sharc/crush/index.htm

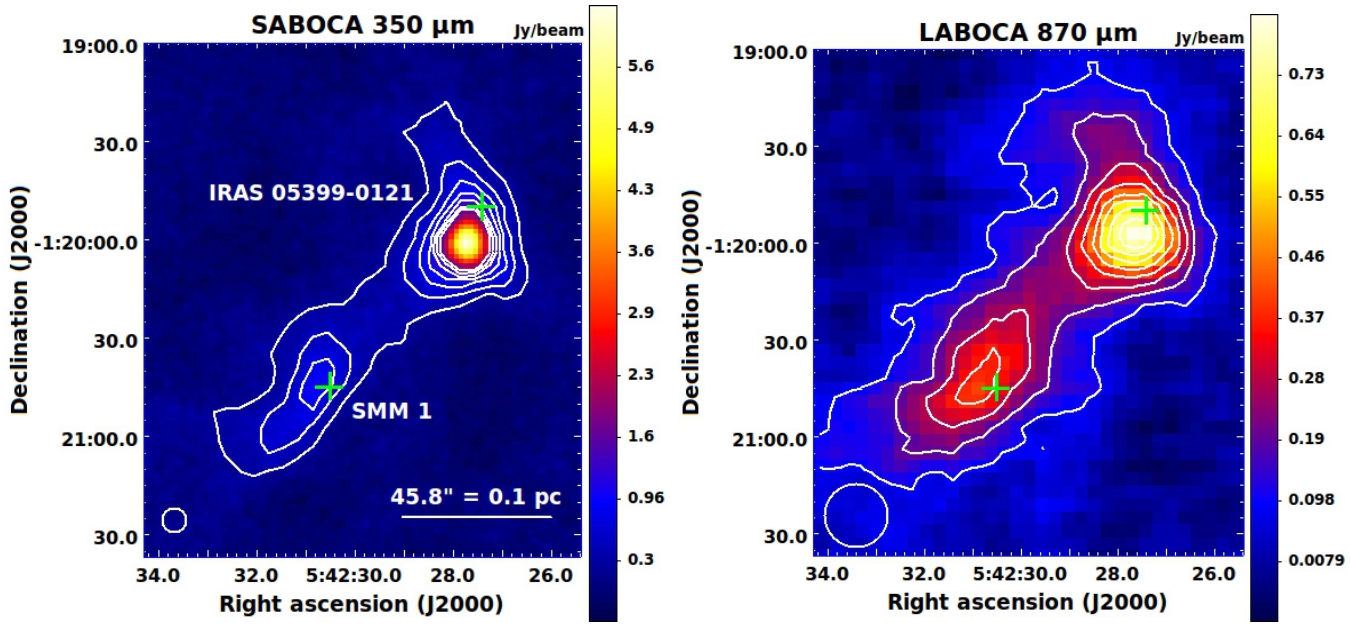

Fig. 1. SABOCA 350-μm and LABOCA 870-μm images of the I05399/SMM 1-system. The images are shown with linear scaling, and the colour bars indicate the surface-brightness scale in Jy beam^{-1}. The overlaid SABOCA contours start at three times the noise level (3σ = 240 mJy beam^{-1}) and increase at this interval to 1680 mJy beam^{-1}. The LABOCA contour levels range from 90 mJy beam^{-1} (3σ) to 720 mJy beam^{-1}, increasing in steps of 3σ. The green plus signs show the target positions of our previous molecular-line observations. A scale bar indicating the 0.1 pc projected length is shown in *the left panel*, with the assumption of a 450 pc line-of-sight distance. The effective beam sizes (7.″63 for SABOCA, 19.″86 for LABOCA) are shown in the *lower left corner of the panels*.

data-reduction software, and to be properly comparable with our present SABOCA data, we re-reduced the LABOCA data with CRUSH-2. Smoothing with a Gaussian kernel of the size 3.″76 was applied, while the instrument beam FWHM used in CRUSH-2 is 19.″5. Therefore, the angular resolution of the final image is 19.″86 (0.043 pc at 450 pc). The gridding was performed with a cell size of 4.″0. The resulting 1σ rms noise level in the final map is 30 mJy beam^{-1}. For comparison, in Paper I the resolution and rms noise were 20.″13 and 30 mJy beam^{-1}. The resulting peak surface brightnesses of the sources are very similar to the values in the BoA-reduced map.

In Paper III, we noticed that our LABOCA map employed in Papers I and II was misaligned, and therefore we had to adjust its pointing (see footnote 2 in Paper III). The target positions of our previous molecular-line observations were chosen to be the peak positions of the LABOCA map before adjusting the pointing, and therefore they are slightly offset from the 870-μm maxima. The misalignment of the map appears to be the result of our data reduction with BoA. In the present work, where the LABOCA data is re-reduced with CRUSH-2, there is a good agreement between the coordinates of the SABOCA and LABOCA peak positions (Sect. 3.2).

2.3. Archival data from the Spitzer space telescope

In this study, we also employ the infrared data from *Spitzer* (Werner et al. 2004) to characterise the star-formation activity in the I05399/SMM 1-system. The *Spitzer* Science Center (SSC)[3] and Infrared Science Archive (IRSA)[4] recently announced the release of a set of Enhanced Imaging Products (SEIP) from the *Spitzer* Heritage Archive (SHA)[5]. These include Super Mosaics and a Source List of photometry for compact sources.

The IRAC (Infrared Array Camera) Super Mosaics were downloaded from SHA. The IRAC instrument took simultaneous images at wavelengths of 3.6, 4.5, 5.8, and 8.0 μm with an angular resolution between 1.″5 and 1.″9 (Fazio et al. 2004). We also retrieved the 24- and 70-μm MIPS (Multiband Imaging Photometer for *Spitzer*; Rieke et al. 2004) images towards I05399/SMM 1. The angular resolution at these wavelengths is 6″ and 18″, respectively. The MIPS data are part of the programme "A MIPS Survey of the Orion L1641 and L1630 Molecular Clouds" (PI: G. Fazio; programme name/ID: ORION_MIPS/47; AOR-Key: 12647424).

I05399 is designated as SSTSLP J054227.67-012000.4 in the Source List. In the 3.″8 diameter aperture, the reported IRAC flux densities in mJy are 1.317 ± 0.005 (3.6 μm), 5.915 ± 0.001 (4.5 μm; bandfill value), 7.195 ± 0.006 (5.8 μm; bandfill), and 9.796 ± 0.018 (8.0 μm). The 24-μm flux density, from a PSF fitting method, is 1.153 ± 0.524 Jy. The latter is close to the value 1.3 ± 0.05 Jy determined in Paper I.

3. Observational results

3.1. Images

The SABOCA and LABOCA images are shown in Fig. 1. The overall filamentary emission morphology seen in the maps is rather similar to each other. The projected length along the long axis of the 350-μm filament is about 2′ or 0.26 pc. The projected average width of this filament is about ∼30″ or ∼0.07 pc. Its aspect ratio is therefore roughly $A \simeq 4$. The projected separation between the 350-μm peaks of I05399 and SMM 1 is ∼1.′1 or 0.14 pc.

[3] http://ssc.spitzer.caltech.edu/
[4] http://irsa.ipac.caltech.edu/
[5] http://sha.ipac.caltech.edu/applications/Spitzer/SHA/

Table 1. SABOCA 350- and LABOCA 870-μm characteristics of I05399 and SMM 1.

Source	λ [μm]	$\alpha_{2000.0}$ [h:m:s]	$\delta_{2000.0}$ [°:′:″]	$R_{\rm eff}$ [″]	$R_{\rm eff}$ [pc]	$I_\nu^{\rm peak}$ [Jy beam^{-1}]	S_ν [Jy]
IRAS 05399-0121	350	05 42 27.7	−01 20 00.4	19.3	0.042	6.24 ± 1.87	20.66 ± 6.20
	870	05 42 27.7	−01 19 57.0	35.3	0.077	0.82 ± 0.09	2.09 ± 0.21
SMM 1	350	05 42 30.9	−01 20 45.4	18.7	0.041	1.03 ± 0.32	7.96 ± 2.39
	870	05 42 30.9	−01 20 45.0	33.1	0.072	0.40 ± 0.05	1.49 ± 0.15

The *Spitzer* images are shown in Figs. 2 and 3. As can be seen from the images, I05399 is associated with 24- and 70-μm point sources, whereas SMM 1 shows no such emission. As described in Sect. 1, I05399 drives the HH 92 protostellar jet. In the *Spitzer*/IRAC three-colour image, we have labelled several of the outflow features associated with HH 92 (see Bally et al. 2002; Table 1 therein). The very long length of the outflow could mean that we are viewing I05399 from an edge-on orientation so that the outflow lies in the plane of the sky. The 4.5-μm band is particularly useful for studying protostellar jets as it is sensitive to shock-excited line features (H_2 and CO; see, e.g., Smith & Rosen 2005; Ybarra & Lada 2009; De Buizer & Vacca 2010). From the base to the northwest tip of the HH 92 jet, a chain of several 4.5-μm knots are apparent. The brightest H_2 knot reported by Bally et al. 2002, is also associated with a strong 4.5-μm feature. These knots might be the result of internal shocks within the jet. The knot HH 91A, showing extended 4.5-μm emission, is a large shock front, and the 4.5-μm features of HH 93 show other shocks associated with the counterflow (in Fig. 2 we have labelled the closest point to I05399 and the brightest knot of HH 93). A visual inspection of the 3.6- and 4.5-μm images provides hint of a quadrupolar outflow, supporting the suggestion that I05399 is actually a binary system.

3.2. The submm cores

To extract the 350- and 870-μm core properties, we employed the commonly used two-dimensional Clumpfind algorithm, `clfind2d`, developed by Williams et al. (1994). The algorithm requires two configuration parameters: *i)* the intensity threshold, i.e., the lowest contour level, which determines the minimum emission to be included into the core; and *ii)* the contour level spacing, which determines the required "contrast" between two cores to be considered as different objects. We set both of these parameters to 3σ or 240 mJy beam^{-1} for SABOCA and 90 mJy beam^{-1} for LABOCA. Blended source structures are assigned via a friends-of-friends algorithm to the closest emission peak. The stepsize used for contouring the data can affect the total number of identified structures: if contour spacings are too large real fragments can be missed, while closely spaced contours can cause artificial noise features to be identified as "real" objects (Pineda et al. 2009). However, our source is relatively simple and the Clumpfind results are therefore expected to be robust. Moreover, Pineda et al. (2009) concluded that that the 2D version of Clumpfind used here is more reliable than the three-dimensional version.

The J2000.0 coordinates of the peak emission, angular and linear core effective radii ($R_{\rm eff} = \sqrt{A_{\rm proj}/\pi}$, where $A_{\rm proj}$ is the projected area within the 3σ contour), peak surface brightnesses, and integrated flux densities (within 3σ) are listed in Cols. (3)−(8) of Table 1. The effective radii listed in Table 1 are not corrected for beam size. The quoted flux density uncertainties were derived from the rms noise and the absolute: calibration error (30% for SABOCA and 10% for LABOCA), which were combined quadratically. We would like to point out that the LABOCA emission peak of I05399 lies 8.″8 southeast of the previously determined position (in the BoA-reduced map), whereas for SMM 1 the revised maximum lies 6″ to the east.

4. Analysis and results

4.1. Dust temperature and H_2 column density maps

The present 350-μm data together with our previous 870-μm data allow us to determine the dust colour temperature ($T_{\rm dust}$) and H_2 column density [$N(H_2)$] distributions in the I05399/SMM 1-system.

We smoothed the SABOCA map to the resolution of our LABOCA data (7.″63 → 19.″86), and regridded the maps to the same pixel size (4″). Convolving the SABOCA map halved the 1σ rms noise level to 40 mJy beam^{-1}. The intensity ratio map was then converted into a $T_{\rm dust}$ map with the dust emissivity index fixed to $\beta = 1.8$. The choice of this value of β, which lies between the usual fiducial values of $\beta = 1$−2, is explained below. Fitting β would require more than two photometric bands, particularly on the Rayleigh-Jeans side of the SED (e.g., Doty & Leung 1994; Shetty et al. 2009). Unfortunately, the SCUBA Legacy 450-μm map does not cover the I05399/SMM 1-system completely (about half of SMM 1 lies outside the map's boundaries). The Orion B9 region was observed as part of the *Herschel* Gould Belt Survey (HGBS) (André et al. 2010)[6]. Besides the value of β and the paucity of wavelength bands used, another important factor affecting the derived dust colour temperatures is that our 870-μm continuum data could be significantly contaminated by the ^{12}CO(3−2) line emission at 345 GHz (Drabek et al. 2012). Although CO does not appear to be significantly depleted in the studied source (Bergin et al. 1999; Paper III), the CO contamination is not expected to be more than a few tens of percent. Mapping observations of CO(3−2) would be required to quantify this effect. The constructed map of line-of-sight-averaged dust temperature is shown in the left panel of Fig. 4.

[6] *Herschel* is an ESA space observatory with science instruments provided by European-led Principal Investigator consortia and with important participation from NASA (Pilbratt et al. 2010). The HGBS is a *Herschel* key programme jointly carried out by SPIRE Specialist Astronomy Group 3 (SAG 3), scientists of several institutes in the PACS Consortium (CEA Saclay, INAF−IFSI Rome and INAF−Arcetri, KU Leuven, MPIA Heidelberg), and scientists of the *Herschel* Science Center (HSC). For more details, see `http://gouldbelt-herschel.cea.fr`. At the moment, the unpublished Level-2 map products are available in the *Herschel* Science Archive (HSA)[7] but these data do not have an absolute intensity level (M. Hennemann, priv. comm.). Unlike *Herschel*, the ground-based bolometers SABOCA and LABOCA heavily filter the emission on large scales in order to remove the atmospheric emission. Because of the current quality of the *Herschel* data on I05399/SMM 1, we do not employ them in the present study.

[7] `http://herschel.esac.esa.int/Science_Archive.shtml`

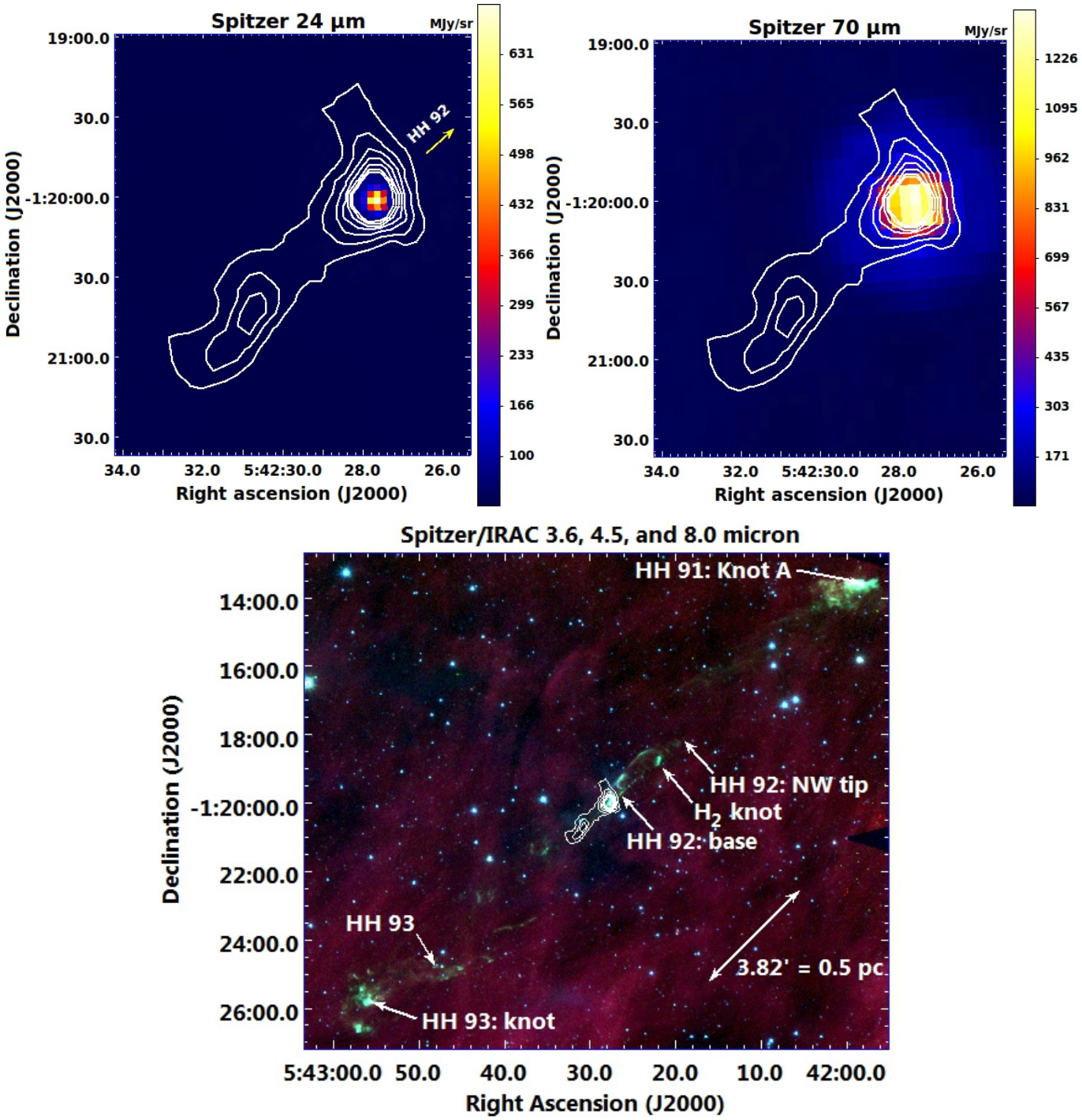

Fig. 2. *Top panels*: *Spitzer*/MIPS 24- and 70-μm images of the I05399/SMM 1-system. The images are shown with linear scaling, and the colour bars indicate the surface-brightness scale in MJy sr^{-1}. The images are overlaid with contours of SABOCA 350-μm dust continuum emission as in Fig. 1. In *the left panel*, the yellow arrow starts from the base of the HH 92 jet driven by I05399 (Bally et al. 2002). *Bottom panel*: *Spitzer*/IRAC three-colour composite image showing the I05399/SMM 1-system in the centre and part of the outflow features associated with the HH 92 jet. The 3.6, 4.5, and 8.0 μm emission is coded in blue, green, and red, respectively, and the colours are shown in logarithmic scales. The contours show the 350-μm emission as in *the top panels*. A scale bar indicating the 0.5 pc projected length is indicated. Note that the total length of the outflow, 34′, corresponds to 4.45 pc at 450 pc.

As expected, I05399 appears as a warm spot with $T_{\rm dust}$ values up to ~ 50 K in the temperature map due to embedded heating source. A higher β value would lower the temperature for the same flux density ratio. Within the aperture with size equal to the effective 350-μm angular size ($R_{\rm eff}$ = 19.″3), and centred on the SABOCA peak, the average $T_{\rm dust}$ towards I05399 is 22.3 ± 10.2 K, where the ±-error represents the standard deviation (hereafter referred to as std). This is comparable to the value ~18.5 K obtained from the SED fit in Paper I. On the other hand, the mean and std of $T_{\rm dust}$ is 15.3 ± 7.0 K in a 40″-diameter aperture centred on the position of our previous NH_3 measurements with 40″ resolution (Paper II). This is close to the measured gas

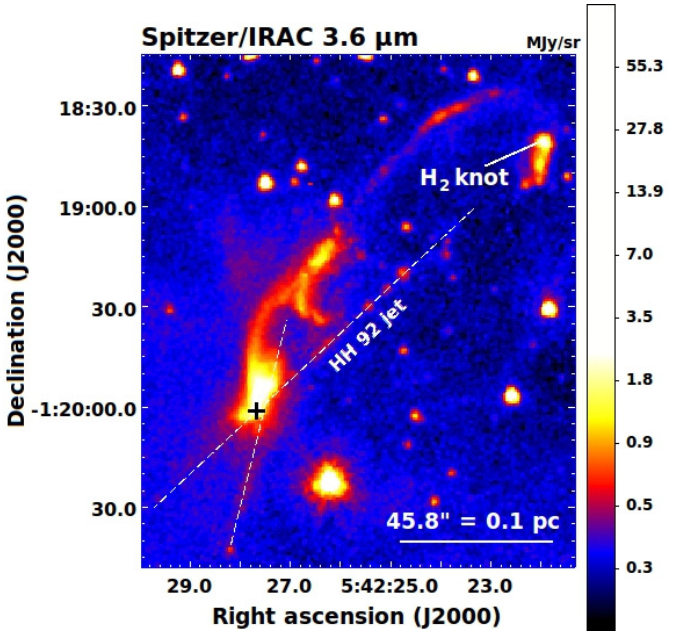

Fig. 3. A zoomed in view of Fig. 2 to show the *Spitzer*/IRAC 3.6-μm emission towards I05399. The image is displayed with logarithmic scaling to highlight the jet features. The dashed lines illustrate the possible quadrupolar outflow structure. Note that SMM 1 lies outside the image. The black plus sign shows the peak of the 24-μm source.

temperature of 13.5 ± 1.6 K. As can be seen in Fig. 4, the temperature is colder in other parts of the system. Measuring $T_{\rm dust}$ within $R_{\rm eff}$ = 18.″7 and centred on the SABOCA peak of SMM 1, the mean±std is 12.5 ± 1.2 K. Towards our line observation position, the corresponding value is 11.4 ± 3.0 K within a 40″ aperture. This is strikingly similar to the $T_{\rm kin}$ value of 11.9 ± 0.9 K derived from ammonia. The $T_{\rm dust}$ rises to ∼15−16 K at the south-eastern edge of the source.

The $N(H_2)$ map was constructed as follows. We first computed the optical thickness map at 870 μm. The $\tau_{870\,\mu{\rm m}}$ map was then divided by the 870-μm dust extinction cross-section per H_2 molecule (cf. Eq. (9) in Miettinen et al. 2010). We adopted the solar abundances for hydrogen, helium, and heavier elements, i.e., their mass fractions were taken to be 0.71, 0.27, and 0.02 of the total mass of all elements, respectively. This corresponds to a helium to hydrogen abundance ratio of about 0.10 and mean molecular weight per H_2 molecule of $\mu_{H_2} \simeq 2.82$ (Kauffmann et al. 2008; Appendix A.1 therein). The 870-μm dust mass absorption (or emission) coefficient, i.e., dust opacity per unit dust mass was taken to be 1.38 cm^2 g^{-1}. This value was interpolated from the widely used Ossenkopf & Henning (1994, hereafter OH94) model describing graphite-silicate dust grains that have coagulated and accreted *thin*[8] ice mantles over a period of 10^5 yr at a gas density of $n_{\rm H} = n({\rm H}) + 2n(H_2) \simeq 2n(H_2) = 10^5$ cm^{-3}. For the average dust-to-hydrogen mass ratio, $M_{\rm dust}/M_{\rm H}$, we adopted the canonical value 1/100 (e.g., Draine 2011; Table 23.1 therein), although the true value can be different (e.g., Vuong et al. 2003; Draine et al. 2007). The total dust-to-gas mass ratio used is therefore $M_{\rm dust}/M_{\rm gas} = M_{\rm dust}/(1.41\ M_{\rm H}) = 1/141$, where the factor 1.41 (≃1/0.71) is the ratio of total mass (H+He+metals) to hydrogen mass. In the adopted OH94 dust model, $\beta \simeq 1.8$, as determined from the slope between 350 and 1300 μm ($\kappa_\lambda \propto \lambda^{-\beta}$). Therefore, this value was adopted in the derivation of the $T_{\rm dust}$ map to be consistent with the dust properties used. The resulting column density map is shown in the right panel of Fig. 4. Both I05399 and SMM 1 stand out as dense portions of the filamentary structure. The $N(H_2)$ values towards these two cores are ∼5−6 × 10^{22} and ∼3−4 × 10^{22} cm^{-2}, respectively.

[8] In Papers I–III, we assumed that the grains have thick ice mantles, and used the 870-μm opacity of $\kappa_{870\,\mu{\rm m}} \simeq 1.7$ cm^2 g^{-1} from OH94. The assumption of thin ice mantles is supported by the fact that no significant CO depletion was found in Paper III.

4.2. Distribution of the dust emissivity index

We can also estimate the value of the dust emissivity index by employing a constant value for the dust temperature (e.g., Schnee & Goodman 2005). As mentioned in Sect. 1., Harju et al. (1993) found that the average gas temperature in the I05399/SMM 1-system is 13.8 ± 3.6 K, without significant variation between different parts within the errors (J. Harju, priv. comm.). Indeed, the $T_{\rm kin}$ values determined in Paper II towards I05399 and SMM 1 are both close to this average value. Therefore, it seems rather reasonable to assume that the average dust temperature of the system is about 13.8 K. The derived emissivity spectral index map is shown in Fig. 5.

Measuring again the values towards the 350-μm peaks with aperture sizes corresponding to the core effective sizes, we obtain the average β values of 2.2 ± 0.4 and 1.6 ± 0.2 for I05399 and SMM 1, respectively. These values are physically reasonable, and, within the errors, comparable to value $\beta = 1.8$ adopted above.

4.3. Core masses, and H_2 column and volume-averaged number densities

The core masses, M, over an effective area of radius $R_{\rm eff}$ were estimated from the integrated 350- and 870-μm flux densities using the standard optically thin dust emission formulation (see, e.g., Eq. (2) in Paper I). As the dust temperature we used the average values 22.3 ± 10.2 K and 12.5 ± 1.2 K for I05399 and SMM 1, respectively. Following the OH94 dust model described above (thin ice mantles), the dust opacity per unit dust mass at 350 and 870 μm was taken to be $\kappa_{350\,\mu{\rm m}} = 7.84$ cm^2 g^{-1} and $\kappa_{870\,\mu{\rm m}} = 1.38$ cm^2 g^{-1}. The total dust-to-gas mass ratio was taken to be 1/141. The uncertainty in mass was propagated from the uncertainty in flux density, and for SMM 1 also from that of the temperature (the large std of $T_{\rm dust}$ for I05399 was not taken into account). The uncertainty in dust opacity, which is likely being a factor ≳2, is the major source of error in the mass estimate.

Besides the values extracted from the $N(H_2)$ map above, we also computed the peak beam-averaged H_2 column densities from the peak surface brightnesses in a standard way (see, e.g., Eq. (3) in Paper I). The parameters needed in the calculation ($T_{\rm dust}$, μ_{H_2}, κ_λ, $M_{\rm dust}/M_{\rm gas}$) were the same as described above. The error in $N(H_2)$ is based on the uncertainty in the peak surface brightness, and for SMM 1 also on the $T_{\rm dust}$ uncertainty. Similarly to mass calculation, the κ_λ uncertainty is likely to be the main source of error here.

The volume of a sphere-averaged H_2 number densities over $R_{\rm eff}$, $\langle n(H_2)\rangle$, were calculated using Eq. (1) of Paper III, and the corresponding errors were propagated from those of M. The masses and densities derived above are listed in Cols. (4)−(6) of Table 2. The core masses derived from 350-μm data are about half the values derived from the lower resolution 870-μm data. On the other hand, the column and number densities derived from 350-μm data are typically about three times higher compared to those derived from LABOCA data.

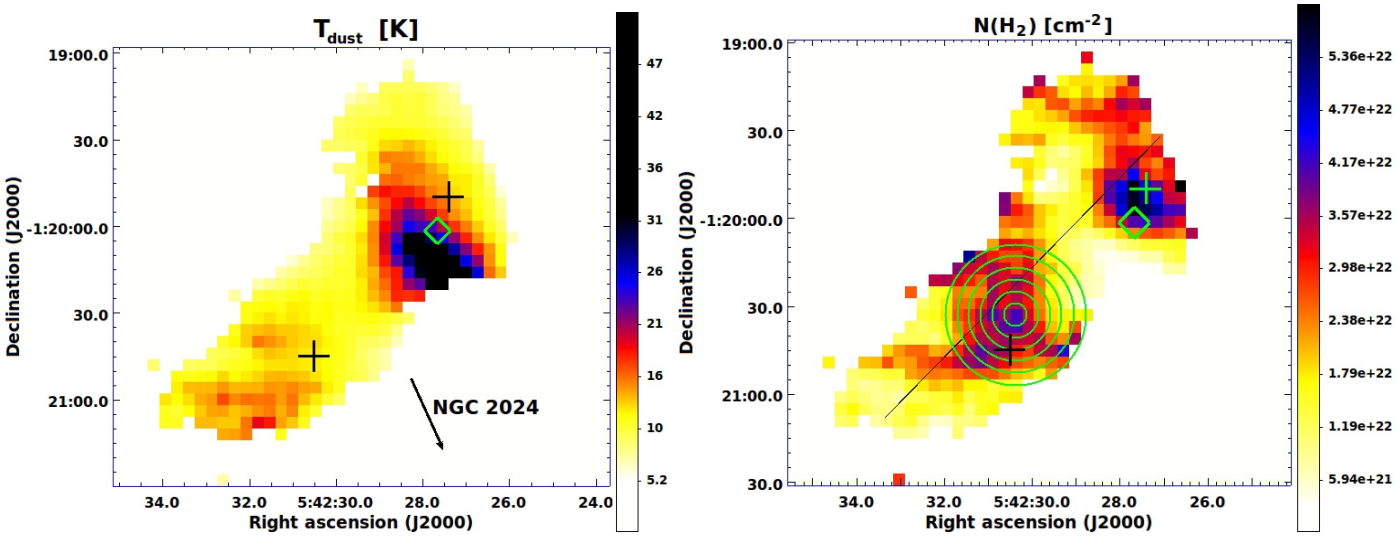

Fig. 4. Distributions of dust colour temperature (*left*) and H_2 column density (*right*). The dust emissivity index, β, was fixed at 1.8. The colour-scale bars on the right indicate the units in K and cm^{-2}, respectively. The plus signs show the target positions of our previous molecular-line observations. The diamond symbol indicates the 24-μm emission peak of I05399. The direction towards NGC 2024 is indicated by an arrow in *the left panel*. The annuli used to compute the density profile shown in Fig. 6 are shown by the green circles, while the black solid line in *the right panel* shows the location of the slice used to extract the central column density discussed in Sect. 4.5. The resolution of the images is 19.″86 or about 0.043 pc.

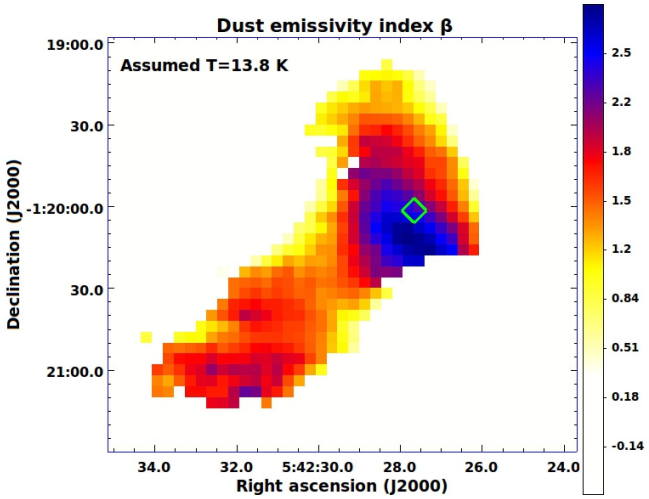

Fig. 5. Distribution of the dust emissivity spectral index with the assumption that the dust temperature is constant at 13.8 K (=$\langle T_{\rm kin}\rangle$; Harju et al. 1993). The diamond symbol indicates the 24-μm emission peak of I05399.

We also constructed a column density distribution using azimuthally averaged values (see Fig. 6). As shown in Fig. 4, the 4″– or one pixel-wide annuli were concentric circles centred on the $N(H_2)$ peak of SMM 1 at $(\alpha, \delta)_{2000.0}$ = 5$^{\rm h}$42$^{\rm m}$30.$^{\rm s}$37, −1°20′32.″95. The radial $N(H_2)$ distribution is presented in Fig. 6. In order to characterise the structure, the data points were fitted[9] with the function (cf. Eq. (15) in Nielbock et al. 2012)

$$N(\mathrm{H_2}) = \frac{N(\mathrm{H_2})_0}{1 + \left(\frac{r}{r_0}\right)^m}, \quad (1)$$

where $N(H_2)_0$ is the central peak column density, r is radial distance, r_0 is the radius of the flat inner region, and m is the power-law exponent at large radii ($r \gg r_0$). The obtained values are $N(\mathrm{H_2})_0 = \left(4.1^{+1.7}_{-1.1}\right) \times 10^{22}$ cm^{-2}, $r_0 = 28.''3^{+11.''6}_{-7.''6} \simeq 0.06^{+0.03}_{-0.01}$ pc, and $m = 1.3^{+2.2}_{-0.9}$. We note that r_0 is only roughly comparable to the thermal Jeans length at the centre of the annuli, i.e., $\lambda_{\rm J} \simeq 0.01 \pm 0.004$ pc at $T = 11.9 \pm 0.9$ K (see, e.g., Arzoumanian et al. 2011; cf. Sect. 4.5). In the case of a simple spherical source with a power-law volume (number) density profile of the form $n(H_2) \propto r^{-p}$, the column density is expected to follow the relation $N(H_2) \propto r^{-m}$ with $m = p - 1$ (e.g., Yun & Clemens 1991). In our case, the density profile would then be $n(H_2) \propto r^{-\left(2.3^{+2.2}_{-0.9}\right)}$. The deconvolved size of SMM 1, when determined from the LABOCA image [whose resolution equals that of the $N(H_2)$ map], is very close to the beam size 19.″9. Interestingly, when this fact is compared with the density power-law distribution models from Young et al. (2003; their Fig. 27), a value of $p \simeq 1.9$ would be expected, not far from the value deduced above (cf. Sect. 5.3 in Paper I).

4.4. Modelling the spectral energy distribution of IRAS 05399-0121

To characterise the physical properties of I05399, we constructed its SED by combining the *Spitzer* photometric data with the submm data from SABOCA, LABOCA, and SCUBA. We also employed the *IRAS* flux densities (see Table 1 in Paper I), for which a typical uncertainty of 10% was adopted. Di Francesco et al. (2008) reported a rather large 850-μm effective radius for I05399, namely 49.″4. The reported SCUBA flux densities are therefore likely to include contributions from SMM 1 also. For this reason, we used apertures of the size corresponding to the effective 350- and 870-μm core sizes to extract the 450- and 850-μm flux densities, respectively. The obtained values are 11.06 ± 5.53 and 2.59 ± 0.52 Jy, where the quoted uncertainties represent the 50% and 20% absolute flux uncertainties, respectively.

To build the SED, we used the SED fitting tool developed by Robitaille et al. (2006, 2007)[10]. The tool employes a grid

[9] We used the non-linear least squares IDL fitting routine MPFIT (Markwardt 2009) available at http://purl.com/net/mpfit

[10] The SED fitter is publicly available at http://caravan.astro.wisc.edu/protostars/

Table 2. Dust colour temperatures, masses, beam-averaged peak H_2 column densities, and volume-averaged H_2 number densities of the cores.

Source	$\langle T_{\rm dust}\rangle$ [K]	λ [μm]	M [$M_\odot$]	$N(H_2)$ [10^{22} cm^{-2}]	$\langle n(H_2)\rangle$ [10^4 cm^{-3}]
IRAS 05399-0121	22.3 ± 10.2	350	2.1 ± 0.6	8.9 ± 2.7	12.9 ± 3.7
		870	3.8 ± 0.4	3.1 ± 0.3	3.8 ± 0.4
SMM 1	12.5 ± 1.2	350	3.8 ± 1.7	7.0 ± 3.2	25.2 ± 11.3
		870	6.7 ± 1.3	3.8 ± 0.8	8.2 ± 1.6

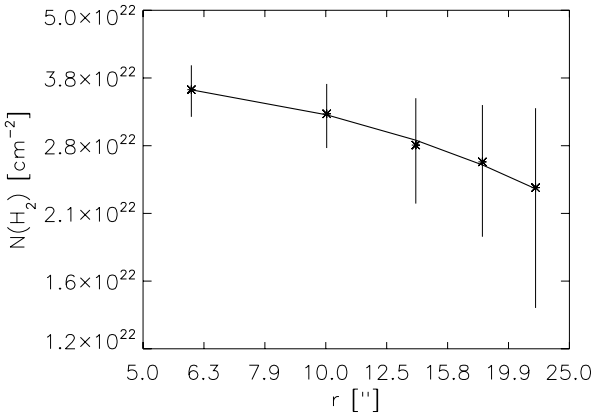

Fig. 6. Radial profile of the column density of SMM 1 displayed with logarithmic scale for both axes. The data points represent azimuthally averaged values inside 4″ wide annuli (Fig. 4). The vertical error bars reflect the standard deviation of the azimuthal averaging. The mean radial $N(H_2)$ profile can be fitted by a power-law with $N(H_2) \propto r^{-(1.3^{+2.2}_{-0.9})}$ between the flat inner core and the "edge", as indicated by the thick solid line.

of two-dimensional axisymmetric radiative-transfer models of YSOs (Whitney et al. 2003) to fit the input flux densities. The grid encompasses a wide range of stellar masses (0.1−50 $M_\odot$; mainly covering low-mass YSOs) and YSO evolutionary stages (stellar ages of 10^3−10^7 yr), and makes use of 20 000 sets of 14 physical parameters and 10 different viewing angles (inclinations ranging from edge-on to pole-on or from 90° to 0°), resulting in a total of 200 000 model SEDs. The models assume that the central embedded source is forming as a single star, it is associated with a flared disk, and that the system is surrounded by a dusty envelope with cavities carved by bipolar outflows. Here, a dust-to-gas ratio of 1/100 is assumed. The models take into account the fact that silicate dust can produce the 10- and 18-μm features (stretching of the Si-O bonds and bending of O-Si-O, respectively), but the models do not include the icy grain mantles or PAH emission features at mid-infrared. The model fitter requires the visual extinction and distance ranges within which to fit the observational data. We limited the former to be within the range $A_V = 0 \ldots 8.5$ mag, which is based on the median A_V value towards the NGC 2024 cluster (Haisch et al. 2001), and the distance was restricted to 450 pc.

The SED is presented in Fig. 7. The best fit is shown by a black curve, whereas the grey curve shows the next-best fit satisfying the criterion $\chi^2 - \chi^2_{\rm best} < 5N_{\rm data}$, where $N_{\rm data} = 13$ is the number of flux data points. The fit to the stellar photosphere SED is shown by a dashed line. Due to possible contamination by shock emission, the *Spitzer*/IRAC 4.5-μm flux density was finally neglected from the fit (it was treated as an upper limit with a zero weight). Inclusion of this data point raised the luminosity to an unrealistically high level (∼230 $L_\odot$). Some other IRAC bands could also be influenced by PAH emission or scattering: the 3.6, 5.8, and 8.0 μm bands contain PAH features at 3.3, 6.2, and 7.7 and 8.6 μm, respectively (Draine 2003), and the 3.6-μm emission can originate from scattered interstellar radiation (Steinacker et al. 2010). The *IRAS* 60- and 100-μm flux densities appear to be slightly inconsistent with the *Spitzer* 70-μm flux density measured by PSF fitting in Paper I. This is likely to result from the fact that the *IRAS* beam of a few arcminutes picks up emission from the source surroundings.

The corresponding SED parameters are listed in Table 3. In this table, we give the inclination angle (i), visual extinction between the observer and the outer edge of the circumstellar material (A_V), stellar age, mass, and temperature ($\tau_\star$, $M_\star$, $T_\star$), the rate of mass accretion from the envelope onto the disk ($\dot{M}_{\rm env}$), disk mass ($M_{\rm disk}$), visual extinction of the circumstellar material ($A_V^{\rm circ}$), total luminosity ($L_{\rm tot}$; contributions from the central star and accretion, assuming that all the accretion energy is radiated away), envelope mass ($M_{\rm env}$), and the implied evolutionary stage of the source. We give the best-fit model parameters with errors calculated as difference between the minimum and maximum values that can be derived from the three next-best model fits. We note that all the masses and the mass accretion rate assume a dust-to-gas ratio of 1/100. The source inclination, $31\overset{\circ}{.}8^{+17\overset{\circ}{.}7}$, is roughly consistent with the observed outflow orientation. The best-fit model stellar mass and total luminosity are found to be $M_\star \sim 0.5\ M_\odot$ and $L_{\rm tot} \sim 15.5\ L_\odot$. The latter is corrected for foreground extinction and does not depend on the viewing angle. It is also comparable to the value 21 ± 1.2 $L_\odot$ derived by fitting a two-temperature component modified blackbody to the source SED (Paper I). The envelope mass, $M_{\rm env} \sim 1.5^{+2.1}_{-0.9}\ M_\odot$, determined from the long wavelength emission, is very similar to that derived from the 350-μm flux density alone, especially when the factor of 1.41 difference in the dust-to-gas ratio is taken into account. It is also comparable to the value 2.8 ± 0.3 $M_\odot$ derived for the cold SED component in Paper I (where the dust-to-gas ratio 1/100 was adopted and grains were assumed to have thick ice mantles).

In the case the range of values is very large, the parameter in question is not well constrained (such as the disk mass). I05399 can be classified following the YSO classification scheme of Robitaille et al. (2006). The evolutionary stage given in the last row of Table 3 is based on the values of $\dot{M}_{\rm env}$ and $M_{\rm disk}$ relative to $M_\star$. I05399 has $\dot{M}_{\rm env}/M_\star \simeq 1.4 \times 10^{-4} > 10^{-6}$ yr^{-1}, and is therefore a Stage I candidate (dominated by a large accreting envelope). This stage is taken to encompass both the Stage 0 (i.e., 30-K modified black-body SED)[11] and I sources (Robitaille et al. 2006). The earliest evolutionary stage 0 is characterised by an envelope whose mass is higher than those of the central star

[11] The Robitaille et al. (2006) SED models do not take into account the cold envelope material (≲30 K), which might have some effect on the longer wavelength fits (see also Offner et al. 2012b). Therefore, the mass of the coldest envelope parts are neglected.

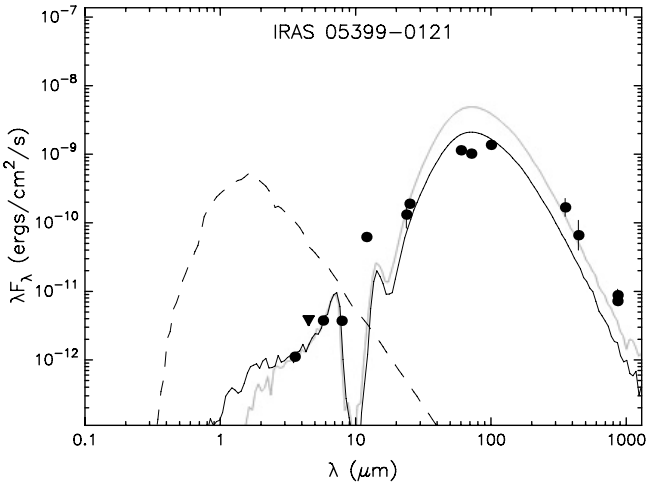

Fig. 7. Spectral energy distribution (SED) of I05399. The filled black circles associated with vertical error bars represent the *Spitzer*, *IRAS*, SABOCA, SCUBA, and LABOCA flux densities. The downwards pointing triangle indicates the *Spitzer*/IRAC 4.5-μm flux density considered as an upper limit (not taken into account in the fit). The solid black line indicates the model that gives the best fit to the input flux densities, whereas the grey line illustrates the subsequent good fit model with the criterion $\chi^2 - \chi^2_{\rm best} < 5$, where χ^2 is taken per data point ($N_{\rm data} = 13$). The black dashed curve shows the SED of the stellar photosphere corresponding to the central source of the best-fitting model (as it would appear in the absence of circumstellar dust, but including the effects of interstellar dust). Note the presence of silicate absorption features at 10 and 18 μm.

Table 3. Results of SED modelling of IRAS 05399-0121.

Parameter	Value[a]
Min. $\chi^2/N_{\rm data}$	$103.6^{+36.3}$
Inclination, i [°]	$31.8^{+17.7}$
Visual extinction, $A_{\rm V}$ [mag]	$2.2^{+2.2}_{-1.4}$
Stellar age, $\tau_\star$ [10^3 yr]	$6.3^{+8.4}_{-5.2}$
Stellar mass, $M_\star$ [$M_\odot$]	$0.46^{+1.09}$
Stellar temperature, $T_\star$ [10^3 K]	$3.65^{+0.53}$
Envelope accretion rate, $\dot{M}_{\rm env}$ [10^{-5} $M_\odot$ yr^{-1}]	$6.47^{+9.13}_{-4.35}$
Disk mass, $M_{\rm disk}$ [$M_\odot$]	$0.0352^{+0.1278}_{-0.0345}$
Circumstellar extinction, $A_{\rm V}^{\rm circ}$ [mag]	430^{+376}_{-29}
Total luminosity, $L_{\rm tot}$ [$L_\odot$]	$15.5^{+23.6}_{-8.62}$
Envelope mass, $M_{\rm env}$ [$M_\odot$]	$1.51^{+2.07}_{-0.91}$
Stage	I

Notes. [(a)] For each model parameter, the best-fit value is given with the ± errors computed from the minimum and maximum values obtained from the three next-best model fits. For some parameters, the best-fit value is the lowest one.

and the disk (see McKee & Offner 2010). For I05399 we obtain the $M_{\rm env}/M_\star$ ratio of only ~3, supporting the idea that it is at the Class (or Stage) 0/I borderline. Offner et al. 2012b simulated the formation of low-mass stars including the effects of outflows and radiative heating. They found that while the SED models could correctly identify the evolutionary stage of the synthetic embedded protostars, the disk and stellar parameters inferred from the SEDs could be very different from the actual simulated values. In particular, the fact that I05399 may be a binary system makes many of the derived source properties highly uncertain.

4.5. Fragmentation of the source

To investigate the dynamical state of the detected 350-μm filamentary structure as a whole, we estimated its total mass as

$$M = \mu_{\rm H_2} m_{\rm H} \sum_i \left[N({\rm H_2}) A_{\rm pix} \right]_i , \quad (2)$$

where $m_{\rm H}$ is the mass of a hydrogen atom, $A_{\rm pix}$ is the surface area in one pixel (16 □″), and the sum is over all pixels within the 3σ contour of 350-μm emission. This integration of the mass surface density gives $M \simeq 8.8\ M_\odot$. As the projected length of the source along the long axis is 0.26 pc, the corresponding mass per unit length, or line mass, is $M_{\rm line} \simeq 34\ M_\odot$ pc^{-1}.

As having a filamentary shape, the I05399/SMM 1-system can be considered a cylindrically shaped object. It is therefore interesting to examine if the source's substructure can be understood in the context of cylindrical fragmentation. For an infinite, unmagnetised, isothermal cylinder, the instability (collapse to line singularity) is reached if its $M_{\rm line}$ exceeds the critical equilibrium value of (e.g., Ostriker 1964; Inutsuka & Miyama 1992)

$$M^{\rm crit}_{\rm line} = \frac{2c_{\rm s}^2}{G}, \quad (3)$$

where G is the gravitational constant. Using the average gas temperature of $\langle T_{\rm kin} \rangle = 13.8 \pm 3.6$ K (Harju et al. 1993) and the mean molecular weight per free particle of $\mu_{\rm p} = 2.37$ (Kauffmann et al. 2008)[12] to calculate the sound speed, we derive the value $M^{\rm crit}_{\rm line} \simeq 22 \pm 6\ M_\odot$ pc^{-1}. The I05399/SMM 1-system therefore appears to be a thermally supercritical filament by a factor of 1.5 ± 0.4. If the external pressure is not negligible, as may well be the case for the dynamic Orion B9 region, then $M^{\rm crit}_{\rm line}$ is lower than the above value (e.g., Fiege & Pudritz 2000). On the other hand, if the non-thermal motions are taken into account, i.e., $c_{\rm s}$ is replaced by the effective sound speed $c_{\rm eff} = (c_{\rm s}^2 + \sigma^2_{\rm NT})^{1/2}$, where $\sigma_{\rm NT} \sim c_{\rm s}$ (Paper II), the value of $M^{\rm crit}_{\rm line}$ becomes about two times larger than in Eq. (3) (Fiege & Pudritz 2000). We would like to stress that this includes the assumption that all of the non-thermal motions are providing additional support, similarly to that provided by thermal pressure (Kirk et al. 2013). The fact that our source already contains a protostellar object, i.e., is collapsing, suggests that it should be (slightly) supercritical. We note that the source mass determined from the $N(\rm H_2)$ map suffers from uncertainty in the dust properties (such as the dust-to-gas ratio and dust opacity).

As mentioned in Sect. 3.1, the projected separation between the subcores I05399 and SMM 1 is 0.14 pc at $d = 450$ pc (the spacing ranges from 0.13 to 0.16 pc for the distance range 400−500 pc). In the case the cylinder has $M_{\rm line} = M^{\rm crit}_{\rm line}$ as is roughly the case for our source, the Jeans length along the long axis is (Larson 1985; Hartmann 2002)

$$\lambda^{\rm c}_{\rm J} = \frac{3.94 c_{\rm s}^2}{G \Sigma_0}, \quad (4)$$

where $\Sigma_0 = \mu_{\rm H_2} m_{\rm H} N({\rm H_2})$ is the central surface density. We estimated the central column density to be the average value along the slice shown in Fig. 4 (position angle 135°.6 east of

[12] The classical value of $\mu_{\rm p} = 2.33$ applies for a gas consisting of $\rm H_2$ molecules with 10% He (He/H= 0.1) and a negligible amount of metals.

north), i.e., $\sim 2.6 \pm 1.0 \times 10^{22}$ cm^{-2}, where the uncertainty is given by one standard deviation. The corresponding value of $\lambda_{\rm J}^{\rm c}$ is 0.075 ± 0.035 pc. This is about 1.9 ± 0.9 times lower than the observed value but within the errors they are in reasonable agreement. The system may therefore lie close to the plane of the sky. For comparison, the traditional thermal Jeans length is

$$\lambda_{\rm J} = \sqrt{\frac{\pi c_{\rm s}^2}{G\langle\rho\rangle}}, \quad (5)$$

where $\langle\rho\rangle = \mu_{\rm H_2} m_{\rm H} \langle n({\rm H_2})\rangle$ is the mean mass density (e.g., Kauffmann et al. 2010). If we use the average density of $\sim 6 \pm 1 \times 10^4$ cm^{-3} derived from the 870-μm values listed in Col. (6) of Table 2, we obtain $\lambda_{\rm J} \simeq 0.09 \pm 0.01$ pc. This is also roughly comparable to the observed core separation.

If the *finite* length and diameter of the cylindrical cloud are L and D, respectively, the number of fragments forming due to gravitational instability is expected to be (e.g., Bastien et al. 1991; Wiseman & Ho 1998)

$$N_{\rm frag} = \frac{L}{\lambda_{\rm crit}} = \frac{2\,(L/D)}{3.94} \simeq 0.5A, \quad (6)$$

where $\lambda_{\rm crit} = 1.97D$ is the wavelength of the most unstable perturbation, and A the cylinder's aspect ratio. As mentioned earlier, A is about 4, so one would expect to have two subfragments, in agreement with the two subcores I05399 and SMM 1. Note that the average width of the SABOCA filament, $D \sim 0.07$ pc, yields $\lambda_{\rm crit} \simeq 0.14$ pc, which is in excellent agreement with the observed separation distance.

To conclude, the studied system has likely fragmented into subcores as a result of cylindrical gravitational instability. Considering a filament of radius R, the fragmentation timescale is then expected to be comparable to the radial crossing time, $\tau_{\rm cross} = R/\sigma$, where σ refers to the total velocity dispersion. If we use the average FWHM linewidth of $\Delta v = \sqrt{8\ln 2}\sigma = 0.6$ km s^{-1} from Harju et al. (1993), which is very similar to the $NH_3(1, 1)$ linewidths found in Paper II, the $\tau_{\rm cross}$ for the SABOCA filament is $\sim 1.34 \times 10^5$ yr. If I05399 has accreted mass at a constant rate since the formation of the central protostar, the fragmentation timescale is 21^{+101}_{-12} times longer than the protostar's age inferred from SED modelling (Table 3).

5. Discussion

5.1. Dust properties

As explained in Sect. 4.1, the temperatures measured for the gas component in Paper II are similar to the dust temperatures measured here from the 350-to-870-μm flux density ratios. The similarity between $T_{\rm kin}$ and $T_{\rm dust}$ suggests that the gas and dust are well-coupled. This is not necessarily surprising, because thermal coupling between the gas and dust by collisions is expected at densities $n \gtrsim 10^4$ cm^{-3} (Goldsmith & Langer 1978).

The constructed $T_{\rm dust}$ map shown in Fig. 4 reveals a warm spot towards I05399. Given the presence of an embedded protostar, the increased 350/870-μm flux density ratio is likely dominated by temperature, although it could be partly due to variation in β also. However, the 24-μm peak position and the warmest spot are not exactly coincident, but there is a slight offset of about 9″ between the two. This difference could be caused by the outflow feedback from I05399, namely heating by outflow shocks. Also, the $T_{\rm dust}$ values appear to rise when going southeast of the 350-μm peak of SMM 1. Perhaps this is another reflection of the outflow interaction related to the HH 92 jet. This conforms to the low CO depletion factors and to the detection of deuterated formaldehyde (D_2CO; a species forming on icy grain surfaces) reported in Paper III as described in Sect. 1. It is worth noting, however, that the warmer southern parts of the I05399/SMM 1-system face the direction towards the Flame Nebula NGC 2024, an active massive star-forming region (see Fig. 9 in Miettinen 2012). Even though this could enhance the strength of the local interstellar radiation field and thus provide external dust heating, one would then expect to see a more uniform $T_{\rm dust}$ gradient across the short axis and along the whole source. Therefore, protostellar or shock heating seems more plausible here.

By fixing the value of $T_{\rm dust}$ to 13.8 K, i.e., to the average $T_{\rm kin}$ derived by Harju et al. (1993), we also computed the map of dust emissivity spectral index, β (Fig. 5). The β varies from ~ 1.3 to 2.8 inside the 3σ SABOCA contour. For comparison, through a multiwavelength study of the starless core TMC-1C, Schnee et al. (2010) derived the values $1.7 \leq \beta \leq 2.7$, the most likely one being ~ 2.2. Shirley et al. (2011), by studying the Class 0 source B335, found a relatively steep submm opacity power-law index of $\beta = (2.18{-}2.58)^{+0.30}_{-0.30}$. From Fig. 5 we see that β appears to rise to values >2 towards those parts where $T_{\rm dust}$ is increased. Of course, our present data does not allow to draw any firm conclusions and one must be careful not to overinterpret the current results, but it can still be speculated that the increase of β is caused by the destruction of dust grains. This would be in line with the destructive outflow feedback discussed above. Depending on the velocity of the jet-induced shock, dust grains can be either partially or completely destroyed by sputtering, grain-grain collisions, and shattering (e.g., Jones et al. 1994; Van Loo et al. 2013). Moreover, the processing by both UV photons and cosmic rays can cause non-thermal desorption of volatile species from the icy grain mantles into the gas phase (e.g., Hartquist & Williams 1990; Roberts et al. 2007). However, it is also possible that higher values of β are actually caused by the growth of icy mantles on dust grains (e.g., Schnee et al. 2010a, and references therein), but this seems to contradict the chemical features discussed earlier. Conversely, observational results of small values of β are often interpreted to be indicative of grain growth (e.g., Testi et al. 2003; Draine 2006; Kwon et al. 2009). For example, Kwon et al. (2009) found that for their sample of Class 0 sources $\beta \lesssim 1$, implying larger grain sizes due to gas accretion and/or coagulation. We note, however, that a visual inspection of the *Spitzer*/IRAC 3.6-μm image of I05399 reveals the presence of a coreshine-like emision (Fig. 3). The 3.6-μm coreshine originates in dust-grain scattering of the background radiation, and is an indication of the presence of large, micron-size grains whose abundance is roughly given by the MRN (Mathis et al. 1977) grain-size distribution (Steinacker et al. 2010). For example, Stutz et al. (2010) found this towards the Bok globule CB 244 (coincidentally, it resembles our source in the sense that it contains a Class 0 protostar and a starless core). Finally, the anti-correlation between $T_{\rm dust}$ and β claimed in some observational studies might be artificial and caused by noise effects and $T_{\rm dust}$–β degeneracy instead of being a real physical trend (e.g., Kelly et al. 2012, and references therein).

5.2. IRAS 05399-0121/SMM 1 – a double core system

One of the original aims of the present high-resolution SABOCA study was to search for substructures within I05399 and SMM 1. The fact that SMM 1 remains a single source is consistent with the finding by Schnee et al. (2010b) that none of their 11 starless cores break into smaller components at 5″ resolution. Although,

higher interferometric resolution may be necessary to see substructure at such scales (Offner et al. 2012a).

The I05399/SMM 1-system appears to be a filamentary-type object not far from equilibrium (slightly thermally supercritical), and the origin of the two subcores, projectively separated by 0.14 pc, seems to be caused by cylindrical Jeans-type fragmentation. We have not applied a correction factor for inclination, but the long length of the outflow driven by I05399, and its possible interaction with SMM 1 suggest that the system is aligned close to the plane of the sky.

Although the fragmentation of the studied system can be explained in the context of a self-gravitating isothermal equilibrium filament, the estimated density profile $n(r) \propto r^{-(2.3^{+2.2}_{-0.9})}$, albeit quite uncertain, is shallower than what would be theoretically expected, i.e., $\sim r^{-4}$ (Ostriker 1964; see also Arzoumanian et al. 2011; Pineda et al. 2011). Instead, it is close to the standard singular isothermal sphere profile of $n(r) \propto r^{-2}$ (Shu 1977). However, Fiege & Pudritz (2000) found that most of their models of isothermal filaments that are threaded by helical magnetic fields and are in gravitational virial balance, can yield density profiles that decline like $\sim r^{-1.8}$ to $\sim r^{-2}$ (see also Lada et al. 1999). Similarly, Caselli et al. (2002) found that starless cores can be modelled with radial density profiles of $n(r) \propto r^{-2}$ outside ~0.03 pc, whereas protostellar cores are better described with steeper single power-law density profiles ($p \geq 2$). For comparison, Shirley et al. (2002) modelled seven Class 0 objects using a single power-law density profiles and found that the best-fit power-law index is $p = 1.8 \pm 0.1$. The same density profile ($p = 1.8$) was found by Schnee & Goodman (2005) for TMC-1C through SCUBA 450/850 μm observations, resembling our 350/870 μm analysis.

If both I05399 and SMM 1 were formed simultaneously through fragmentation, it is interesting why they are at so different stages of evolution: the former is already a relatively evolved protostar, while the latter one is still starless. This is not a unique case in this sense; a similar situation holds for the double-core globules CB 26 and 244 recently studied by Launhardt et al. (2013). Also, the filamentary clump associated with the Class 0 protostar IRAS 05405-0117 in Orion B9 shows starless substructure in the $N_2H^+(1-0)$ map by Caselli & Myers (1994) and in submm dust emission maps (Papers I and III). Miettinen (2012) suggested that the core formation in Orion B9 could have been triggered by the feedback from NGC 2024. Externally induced compression could have led to a phase of rapid accretion (Hennebelle et al. 2003; Motoyama & Yoshida 2003), which might be able to explain the advanced evolutionary stage of I05399, but it is unclear why SMM 1 would have not experienced the same fate. The length of the outflow driven by I05399 supports the hypothesis that the central source is a strong accretor. Because I05399 lies at the tip of both the major parent filament (see Fig. 9 in Miettinen 2012) and the smaller scale elongated structure studied here, it could represent a point where gravitational focusing has enabled the rapid evolution into protostellar phase (Tobin et al. 2010). Again, why this would have not happened for SMM 1 remains unclear.

The virial mass we derived for SMM 1 in Paper II is $M_{\rm vir} = 11.1 \pm 0.3\ M_\odot$, where it was assumed that $n(r) \propto r^{-1}$. If this is compared with the revised 870-μm core mass derived here, we obtain the virial parameter $\alpha_{\rm vir} = M_{\rm vir}/M = 1.7 \pm 0.3$ (Bertoldi & McKee 1992). If the density profile of SMM 1 is of the form $n(r) \propto r^{-2.3}$, the above $M_{\rm vir}$ should be divided by a factor of 2.62, and, as a cigar-shaped prolate spheroid with the axial ratio of about 1.8, a further division by a factor of ~0.8 should also be applied (Bertoldi & McKee 1992; Schnee & Goodman 2005). These correction factors yield the value $\alpha_{\rm vir} = 0.8 \pm 0.2$. SMM 1 is therefore very likely to be gravitationally bound ($\alpha_{\rm vir} < 2$) and near virial equilibrium ($\alpha_{\rm vir} = 1$). Also the high density and degree of deuterium fractionation in SMM 1 support its prestellar nature. The fact that I05399 has collapsed faster than SMM 1 could mean that the latter has stronger internal forces resisting gravity. One might also conclude that the outflow from I05399 has triggered the formation of SMM 1, but that it has not collapsed to form a protostar yet.

6. Summary and conclusions

We have mapped the dense core system IRAS 05399/SMM 1 in Orion B9 at 350 and 870 μm using the bolometer cameras SABOCA and LABOCA on APEX. The present study demonstrates the complementarity of these two instruments, similarly to what has been done in other studies using SCUBA at 450 and 850 μm on JCMT. In particular, the present data allowed us to construct the maps of dust colour temperature and column density at relatively high angular resolution (19.″9).

The source is filamentary in shape, and there is a protostellar core at the nortwestern tip (I05399) and a starless core at the southeastern end (SMM 1). By comparing the total line mass of the SABOCA filament to its critical equilibrium value, we conclude that as a whole it is slightly thermally supercritical. The observational fact that there appears to be two subcores projectively separated by 0.14 pc can be understood in terms of Jeans-type cylindrical fragmentation. A simple analysis suggests that the radial density profile is shallower than for an isothermal unmagnetised filament in equilibrium ($\sim r^{-(2.3^{+2.2}_{-0.9})}$ vs. $\sim r^{-4}$).

The SED we constructed for I05399 suggests that it is near the transition phase between Stages 0 and I, in agreement with our previous results. To our knowledge, we have presented the first *Spitzer*/IRAC images of the spectacular outflow driven by I05399. The quadrupolar-type jet morphology seen in the 3.6-μm image supports the possibility that I05399 is actually a binary protostar.

If I05399 and SMM 1 were formed simultaneously through fragmentation of the parent filament, the distinct evolutionary stage between the two could be the result of rapid mass accretion onto I05399 in a high-pressure environment. In principle, this could be the result of core formation triggered by external feedback from NGC 2024 as suggested by Miettinen (2012), but why SMM 1 would not have experienced the same effect is unclear. The temperature map we computed (under the assumption of constant dust opacity spectral index $\beta = 1.8$) shows a few warmer parts, one associated with I05399 and the other at the southeastern end. These could, in part, be imprints of the outflow feedback from I05399, as supported by our earlier results on the chemical properties of the source (e.g., low CO depletion). However, it cannot be excluded that NGC 2024, some ~30′ (~4 pc) southwest of I05399/SMM 1, is proving external heating, although the source's temperature gradient does not support this idea.

One of our original aims here was to search for substructures or dense condensations within the cores. Given the results presented in Paper III (many of the Orion B9 cores are split into substructures consistent with Jeans instability), the high spatial resolution of the present SABOCA data, ~3400 AU, could have revealed some further sub-fragmentation. However, the cores I05399 and SMM 1 do not break up into subcondensations but the system remains a double source at the current resolution.

Acknowledgements. We thank the referee, Paola Caselli, for a thorough reading of the manuscript and providing helpful comments and suggestions. We are grateful to the staff at the APEX telescope for performing the service-mode SABOCA/LABOCA observations presented in this paper. O.M. acknowledges the Academy of Finland for the financial support through grant 132291. S.S.R.O. acknowledges support from NSF Fellowship AST-0901055 and NASA through Hubble Fellowship grant HF-51311. This work is based in part on observations made with the *Spitzer* Space Telescope, which is operated by the Jet Propulsion Laboratory, California Institute of Technology under a contract with NASA. This research has made use of NASA's Astrophysics Data System and the NASA/IPAC Infrared Science Archive, which is operated by the JPL, California Institute of Technology, under contract with the NASA.

References

Aoyama, H., Mizuno, N., Yamamoto, H., et al. 2001, PASJ, 53, 1053
André, P., Ward-Thompson, D., & Barsony, M. 1993, ApJ, 406, 122
André, P., Ward-Thompson, D., & Barsony, M. 2000, in Protostars and Planets IV, eds. V. Mannings, A. P. Boss, & S. S. Russell (Tucson: Univ. of Arizona Press), 59
André, P., Men'shchikov, A., Bontemps, S., et al. 2010, A&A, 518, L102
Arce, H. G., & Sargent, A. I. 2006, ApJ, 646, 1070
Arzoumanian, D., André, P., Didelon, P., et al. 2011, A&A, 529, L6
Bacmann, A., Lefloch, B., Ceccarelli, C., et al. 2003, ApJ, 585, L55
Bally, J., Reipurth, B., & Aspin, C. 2002, ApJ, 574, L79
Bastien, P., Arcoragi, J.-P., Benz, W., et al. 1991, ApJ, 378, 255
Bate, M. R. 2011, MNRAS, 417, 2036
Bergin, E. A., & Langer, W. D. 1997, ApJ, 486, 316
Bergin, E. A., Plume, R., Williams, J. P., & Myers, P. C. 1999, ApJ, 512, 724
Bergman, P., Parise, B., Liseau, R., & Larsson, B. 2011, A&A, 527, A39
Bertoldi, F., & McKee, C. F. 1992, ApJ, 395, 140
Caselli, P., & Myers, P. C. 1994, in Clouds, Cores, and Low Mass Stars, eds. D. P. Clemens, & R. Barvainis, ASP Conf. Ser., 65, 52
Caselli, P., & Myers, P. C. 1995, ApJ, 446, 665
Caselli, P., Walmsley, C. M., Terzieva, R., & Herbst, E. 1998, ApJ, 499, 234
Caselli, P., Benson, P. J., Myers, P. C., & Tafalla, M. 2002, ApJ, 572, 238
Codella, C., Palumbo, G. G. C., Pareschi, G., et al. 1995, MNRAS, 276, 57
Connelley, M. S., Reipurth, B., & Tokunaga, A. T. 2007, AJ, 133, 1528
De Buizer, J. M., & Vacca, W. D. 2010, AJ, 140, 196
Di Francesco, J., Johnstone, D., Kirk, H., et al. 2008, ApJS, 175, 277
Doty, S. D., & Leung, C. M. 1994, ApJ, 424, 729
Drabek, E., Hatchell, J., Friberg, P., et al. 2012, MNRAS, 426, 23
Draine, B. T. 2003, ARA&A, 41, 241
Draine, B. T. 2006, ApJ, 636, 1114
Draine, B. T. 2011, Physics of the Interstellar and Intergalactic Medium (Princeton University Press)
Draine, B. T., Dale, D. A., Bendo, G., et al. 2007, ApJ, 663, 866
Enoch, M. L., Evans, N. J., II, Sargent, A. I., & Glenn, J. 2009, ApJ, 692, 973
Evans, N. J., II, Dunham, M. M., Jørgensen, J. K., et al. 2009, ApJS, 181, 321
Fazio, G. G., Hora, J. L., Allen, L. E., et al. 2004, ApJS, 154, 10
Fiege, J. D., & Pudritz, R. E. 2000, MNRAS, 311, 85
Furuya, R. S. 2003, in Galactic Star Formation Across the Stellar Mass Spectrum, eds. J. M. De Buizer, & N. S. van der Bliek, ASP Conf. Ser., 287, 367
Genzel, R., & Stutzki, J. 1989, ARA&A, 27, 41
Goldsmith, P. F., & Langer, W. D. 1978, ApJ, 222, 881
Güsten, R., Nyman, L. Å., Schilke, P., et al. 2006, A&A, 454, L13
Haisch, K. E., Jr., Lada, E. A., Piña, R. K., et al. 2001, AJ, 121, 1512
Harju, J., Walmsley, C. M., & Wouterloot, J. G. A. 1991, A&A, 245, 643
Harju, J., Walmsley, C. M., & Wouterloot, J. G. A. 1993, A&AS, 98, 51
Hartmann, L. 2002, ApJ, 578, 914
Hartquist, T. W., & Williams, D. A. 1990, MNRAS, 247, 343
Hennebelle, P., Whitworth, A. P., Gladwin, P. P., & André, P. 2003, MNRAS, 340, 870
Ikeda, N., Kitamura, Y., & Sunada, K. 2009, ApJ, 691, 1560
Inutsuka, S.-I., & Miyama, S. M. 1992, ApJ, 388, 392
Jones, A. P., Tielens, A. G. G. M., Hollenbach, D. J., & McKee, C. F. 1994, ApJ, 433, 797
Kauffmann, J., Bertoldi, F., Bourke, T. L., et al. 2008, A&A, 487, 993
Kauffmann, J., Pillai, T., Shetty, R., et al. 2010, ApJ, 712, 1137
Kelly, B. C., Shetty, R., Stutz, A. M., et al. 2012, ApJ, 752, 55
Kirk, H., Myers, P. C., Bourke, T. L., et al. 2013, ApJ, 766, 115
Kovács, A. 2008, Proc. SPIE, 7020, 45
Kwon, W., Looney, L. W., Mundy, L. G., et al. 2009, ApJ, 696, 841
Lada, E. A., Bally, J., & Stark, A. A. 1991, ApJ, 368, 432
Lada, E. A., Evans, N. J., II, & Falgarone, E. 1997, ApJ, 488, 286
Lada, C. J., Alves, J., & Lada, E. A. 1999, ApJ, 512, 250
Larson, R. B. 1969, MNRAS, 145, 271
Larson, R. B. 1985, MNRAS, 214, 379
Launhardt, R., Mezger, P. G., Haslam, C. G. T., et al. 1996, A&A, 312, 569
Launhardt, R., Stutz, A. M., Schmiedeke, A., et al. 2013, A&A, 551, A98
Manoj, P., Watson, D. M., Neufeld, D. A., et al. 2013, ApJ, 763, 83
Markwardt, C. B. 2009, Astronomical Data Analysis Software and Systems XVIII, ASPC, 411, 251
Masunaga, H., & Inutsuka, S.-I. 2000, ApJ, 531, 350
Masunaga, H., Miyama, S. M., & Inutsuka, S.-I. 1998, ApJ, 495, 346
Mathis, J. S., Rumpl, W., & Nordsieck, K. H. 1977, ApJ, 217, 425
McKee, C. F., & Offner, S. S. R. 2010, ApJ, 716, 167
Megeath, S. T., Gutermuth, R., Muzerolle, J., et al. 2012, AJ, 144, 192
Menten, K. M., Reid, M. J., Forbrich, J., & Brunthaler, A. 2007, A&A, 474, 515
Miettinen, O. 2012, A&A, 545, A3
Miettinen, O., & Harju, J. 2010, A&A, 520, A102
Miettinen, O., Harju, J., Haikala, L. K., Kainulainen, J., & Johansson, L. E. B. 2009, A&A, 500, 845 (Paper I)
Miettinen, O., Harju, J., Haikala, L. K., & Juvela, M. 2010, A&A, 524, A91 (Paper II)
Miettinen, O., Harju, J., Haikala, L. K., & Juvela, M. 2012, A&A, 538, A137 (Paper III)
Motoyama, K., & Yoshida, T. 2003, MNRAS, 344, 461
Myers, P. C., Mardones, D., Tafalla, M., et al. 1996, ApJ, 465, L133
Neugebauer, G., Habing, H. J., van Duinen, R., et al. 1984, ApJ, 278, L1
Nielbock, M., Launhardt, R., Steinacker, J., et al. 2012, A&A, 547, A11
Offner, S. S. R., Capodilupo, J., Schnee, S., & Goodman, A. A. 2012a, MNRAS, 420, L53
Offner, S. S. R., Robitaille, T. P., Hansen, C. E., et al. 2012b, ApJ, 753, 98
Ossenkopf, V., & Henning, T. 1994, A&A, 291, 943 (OH94)
Ostriker, J. 1964, ApJ, 140, 1056
Pilbratt, G. L., Riedinger, J. R., Passvogel, T., et al. 2010, A&A, 518, L1
Pineda, J. E., Rosolowsky, E. W., & Goodman, A. A. 2009, ApJ, 699, L134
Pineda, J. E., Goodman, A. A., Arce, H. G., et al. 2011, ApJ, 739, L2
Reichertz, L. A., Weferling, B., Esch, W., & Kreysa, E. 2001, A&A, 379, 735
Rieke, G. H., Young, E. T., Engelbracht, C. W., et al. 2004, ApJS, 154, 25
Roberts, J. F., Rawlings, J. M. C., Viti, S., & Williams, D. A. 2007, MNRAS, 382, 733
Robitaille, T. P., Whitney, B. A., Indebetouw, R., et al. 2006, ApJS, 167, 256
Robitaille, T. P., Whitney, B. A., Indebetouw, R., & Wood, K. 2007, ApJS, 169, 328
Schnee, S., & Goodman, A. 2005, ApJ, 624, 254
Schnee, S., Enoch, M., Noriega-Crespo, A., et al. 2010a, ApJ, 708, 127
Schnee, S., Enoch, M., Johnstone, D., et al. 2010b, ApJ, 718, 306
Schuller, F. 2012, Millimeter, Submillimeter, and Far-Infrared Detectors and Instrumentation for Astronomy, VI. Proc. SPIE, 8452
Shetty, R., Kauffmann, J., Schnee, S., et al. 2009, ApJ, 696, 2234
Shirley, Y. L., Evans, N. J., II, & Rawlings, J. M. C. 2002, ApJ, 575, 337
Shirley, Y. L., Huard, T. L., Pontoppidan, K. M., et al. 2011, ApJ, 728, 143
Shu, F. H. 1977, ApJ, 214, 488
Siringo, G., Kreysa, E., Kovács, A., et al. 2009, A&A, 497, 945
Siringo, G., Kreysa, E., De Breuck, C., et al. 2010, The Messenger, 139, 20
Smith, M. D., & Rosen, A. 2005, MNRAS, 357, 1370
Steinacker, J., Pagani, L., Bacmann, A., & Guieu, S. 2010, A&A, 511, A9
Stutz, A., Launhardt, R., Linz, H., et al. 2010, A&A, 518, L87
Sunada, K., Nakazato, T., Ikeda, N., et al. 2007, PASJ, 59, 1185
Testi, L., Natta, A., Shepherd, D. S., & Wilner, D. J. 2003, A&A, 403, 323
Tobin, J. J., Hartmann, L., Looney, L. W., & Chiang, H.-F. 2010, ApJ, 712, 1010
Tremblin, P., Schneider, N., Minier, V., et al. 2012, A&A, 548, A65
Van Loo, S., Ashmore, I., Caselli, P., et al. 2013, MNRAS, 428, 381
Vázquez-Semadeni, E., Ballesteros-Paredes, J., & Klessen, R. S. 2003, ApJ, 585, L131
Vorobyov, E. I. 2010, ApJ, 713, 1059
Vuong, M. H., Montmerle, T., Grosso, N., et al. 2003, A&A, 408, 581
Ward-Thompson, D., Scott, P. F., Hills, R. E., & André, P. 1994, MNRAS, 268, 276
Werner, M. W., Roellig, T. L., Low, F. J., et al. 2004, ApJS, 154, 1
Whitney, B. A., Wood, K., Bjorkman, J. E., & Wolff, M. J. 2003, ApJ, 591, 1049
Williams, J. P., de Geus, E. J., & Blitz, L. 1994, ApJ, 428, 693
Wiseman, J. J., & Ho, P. T. P. 1998, ApJ, 502, 676
Wouterloot, J. G. A., & Walmsley, C. M. 1986, A&A, 168, 237
Wouterloot, J. G. A., Walmsley, C. M., & Henkel, C. 1988, A&A, 203, 367
Wouterloot, J. G. A., Henkel, C., & Walmsley, C. M. 1989, A&A, 215, 131
Wuchterl, G., & Tscharnuter, W. M. 2003, A&A, 398, 1081
Ybarra, J. E., & Lada, E. A. 2009, ApJ, 695, L120
Young, C. H., Shirley, Y. L., Evans, N. J., II, & Rawlings, J. M. C. 2003, ApJS, 145, 111
Yun, J. L., & Clemens, D. P. 1991, ApJ, 381, 474
Zhou, S. 1992, ApJ, 394, 204